Pure Appl. Geophys. 181 (2024), 2083–2105

https://doi.org/10.1007/s00024-024-03464-6

Pure and Applied Geophysics

Deformation and Frictional Failure of Granular Media in 3D Analog and Numerical Experiments

P. I. Ioannidi,[1,2] S. McLafferty,[1] J. E. Reber,[1] G. Morra,[3] and D. Weatherley[4]

Abstract—Frictional sliding along grain boundaries in brittle shear zones can result in the fragmentation of individual grains, which ultimately can impact slip dynamics. During deformation at small scales, stick–slip motion can occur between grains when existing force chains break due to grain rearrangement or failure, resulting in frictional sliding of granular material. The rearrangement of the grains leads to dilation of the granular package, reducing the shear stress and subsequently leading to slip. Here, we conduct physical experiments employing HydroOrbs, an elasto-plastic material, to investigate grain comminution in granular media under simple shear conditions. Our findings demonstrate that the degree of grain comminution is dependent on both the normal force and the size of the grains. Using the experimental setup, we benchmark Discrete Element Method (DEM) numerical models, which are capable of simulating the movement, rotation, and fracturing of elasto-plastic grains subjected to simple shear. The DEM models successfully replicate both grain comminution patterns and horizontal force fluctuations observed in our physical experiments. They show that increasing normal forces correlate with higher horizontal forces and more fractured grains. The ability of our DEM models to accurately reproduce experimental results opens up new avenues for investigating various parameter spaces that may not be accessible through traditional laboratory experiments, for example, in assessing how internal friction or cohesion affect deformation in granular systems.

Keywords: Granular media, frictional failure, grain comminution, analog experiments, discrete element method.

1. Introduction

In the upper crust, brittle deformation in shear zones is recorded in the fracturing of rocks and the formation of fault rocks such as gouges (Sibson, 1977). In brittle fault zones, cataclasis leads to grain size reduction due to frictional sliding along grain boundaries and fragmentation of individual grains within the shear zone (Marone & Scholz, 1989; Sibson, 1977). Frictional sliding can result in a stick–slip signal where stress builds during sticking events and is subsequently released after the strength of the rock is overcome and displacement occurs (Brace & Byerlee, 1966). At small scales, stick–slip motion can occur between grains during deformation, while at large scales, stick–slip motion between volumes of rock can lead to earthquakes.

In any granular system, stick–slip motion can be linked to the formation and failure of force chains. In a jammed state (the sticking phase), forces are supported by force chains (Cates et al., 1998). During this phase, shear stress increases until grains begin to rearrange or break, initiating the slipping phase. Slip occurs when existing force chains break due to grain rearrangement or failure, resulting in frictional sliding of the granular material. The rearrangement of the grains leads to dilation of the granular package reducing the shear stress, subsequently leading to slip (Cain et al., 2001).

Numerous experimental and numerical studies have investigated deformation dynamics of granular systems during shear deformation in 2-dimensions (2D) and 3-dimensions (3D) (e.g., Daniels & Hayman, 2008; Frye & Marone, 2002; Ladd & Reber, 2020; Mair et al., 2002; Reber et al., 2015; Siman-Tov & Brodsky, 2018), showing that the deformation

P. I. Ioannidi and S. McLafferty contributed equally to this study.

[1] Department of Geological and Atmospheric Sciences, Iowa State University, Ames, IA, USA. E-mail: ioannidi.iop@gmail.com
[2] *Present Address*: Department of Earth Sciences, Vrije Universiteit Amsterdam, Amsterdam, The Netherlands.
[3] Department of Physics, University of Louisiana at Lafayette, Lafayette, LA, USA.
[4] Julius Kruttschnitt Mineral Research Centre, Sustainable Minerals Institute, The University of Queensland, Brisbane, Australia.

of a granular system is directly affected by grain comminution, grain shape, roughness, and particle size distribution (e.g., Mair et al., 2002; Marone & Scholz, 1989). The particle size distribution and particle friction in a deforming 2D granular system impact the formation of particle bridges where high differential stresses are created, leading to the breaking of individual particles due to particle rolling (Morgan & Boettcher, 1999). Another mechanism leading to grain comminution is the rearrangement of grains close to any shear boundary during deformation (Siman-Tov & Brodsky, 2018). Numerical experiments on 3D granular systems show that the grain size distribution is a direct function of accumulated strain and applied normal stress (Abe & Mair, 2005). Guo and Morgan (2006) simulated the comminution process of quartz gouge and examined the influence of grain comminution on the frictional and micromechanical behavior of granular shear zones. Their results show that grain comminution can lead to either a decrease or increase gouge strength, depending on the direction and degree of change in grain shape. In addition, they show that the intensity and probability of grain comminution in narrow grain size gouges are impacted by factors such as grain shape, material strength, and normal stress. Homogeneous grain size distributions in a deforming granular system will gradually evolve into a wider grain size distribution (Mair & Abe, 2008). Two distinct comminution mechanisms, grain splitting and grain abrasion, that are favored for different normal stresses and wall roughness, are responsible for the evolution in grain sizes in granular systems (Mair & Abe, 2011). With an increase in wall roughness, the frictional strength of the system increases and eventually becomes independent of roughness (Shojaaee et al., 2012).

Here, we explore grain comminution in granular media from the perspective of both laboratory and numerical experiments. We present experiments using a new experimental material, HydroOrbs. HydroOrbs are elastic until an elastic yield point is reached, and they fracture and split into smaller pieces. Their original size and elastic yield can be tuned, which makes them a good target material for experiments on grain comminution. We use the experimental setup and results to benchmark Discrete Element Method (DEM) models, which in future steps will allow for an investigation of the parameter space not accessible through physical experiments. In both the physical and the numerical experiments, we deform particles that fracture in simple shear. We use the material and geometrical parameters from the physical experiments as input parameters for the DEM models. We show that the DEM experiments can reproduce qualitatively grain comminution and particle migration as well as the horizontal force fluctuations of the physical experiments. Even though the application of DEM simulations for modeling particle fracturing is not a new concept, this study provides a unique benchmark of the DEM models with physical experiments. This opens the path to systematic investigations of parameters that cannot be easily varied in a laboratory setting, such as friction coefficient and cohesion, which are known to play a major role in fault gouge deformation and slip dynamics. Moreover, with the calibrated numerical models, we gain insight into the fracturing dynamics and micromechanical mechanisms during shearing and grain comminution.

2. Physical Experiments

We conduct a series of granular experiments in a ring shear apparatus where we deform elasto-plastic HydroOrbs. We systematically change the imposed normal force and monitor the failure of individual grains and the deformation dynamics.

2.1. Experimental Setup and Materials

Experiments are conducted in a ring shear apparatus consisting of two concentric cylinders with radii of 11 cm and 19 cm attached to a baseplate. The experimental material is contained in the resulting 8 cm cylindrical annulus at a height of 16 cm. The experimental chamber is capped by a hydraulic lid that allows for control of the normal force acting on the experimental material. Shear of the experimental material is initiated by rotating the baseplate and experimental chamber walls while keeping the lid stationary. Both the lid and the baseplate of the experimental chamber have 1 cm high teeth that span

Table 1

Parameters for the analog experiments

Experiment	Orb type	Orb diameter (cm)	Orb yield stress (kPa)	Max. normal force (N)	Max. confining pressure (kPa)
CL_D1	CL/D	1.69 ± 0.09	25.44 ± 13.96	61.56	0.82
CL_D2	CL/D	1.69 ± 0.09	25.44 ± 13.96	154.00	2.04
CL_T	CL/T	1.41 ± 0.06	21.43 ± 13.81	201.27	2.67
CF_D	CF/D	1.66 ± 0.08	25.62 ± 16.27	161.00	2.14
CF_T	CF/T	1.43 ± 0.08	21.97 ± 15.70	165.52	2.20
CF_LG	LG/T	3.87 ± 0.25	7.07 ± 12.79	67.19	0.89

CL colorless, *CF* colorful, *D* DI water, *T* tap water, *LG* large

All orbs are punctured. The diameters and yield stresses of the orbs used in the experiments are listed including standard deviation. Maximum normal force and confining pressure recorded during the experiment are also listed

the width between the experimental walls to increase the contact area with the experimental material and to transfer the deformation motion. A cylindrical stepper motor mounted around the base of the experimental chamber drives the experimental chamber. The motor is connected to the experimental chamber via a spring that is connected to a force gauge. Adding the spring as an elastic element between the motor and the experimental chamber allows for distinct stick slip and force oscillations to occur (Birren & Reber, 2019; Daniels & Hayman, 2008; Reber et al., 2014). We use a spring with a spring constant of 9712 N/m for all experiments. The pulling force necessary to rotate the experimental chamber is recorded at a rate of 10 Hz, and an average bulk force is calculated for every full rotation of the experimental chamber. The force signal from the deforming material is separated from the machine noise with a moving average filter. To achieve this, the difference between the raw data and the noise filter is calculated at every data point. Then, the variance of the difference values is calculated for each rotation. Larger differences between the raw and filtered data result in larger variance values. This reflects a stronger oscillation of the spring due to the deforming experimental materials. In addition to the pulling force, we measure the normal force applied to the experimental materials with a force gauge mounted to the lid of the apparatus. For a more detailed description of the experimental setup, removal of background noise, and pulling force data treatment see McLafferty et al. (2023).

HydroOrbs or Hydrogel spheres (e.g., Dijksman et al., 2017; James et al., 2020) are used as granular experimental material. HydroOrbs are small, dehydrated spheres (∼ 2 mm in diameter with larger spheres ∼ 4 mm) that, once in contact with water, swell to about ten times their size. Both colorless and colorful HydroOrbs are used in the physical experiments and the orbs expand to different sizes depending on the salinity of the water when submerged (Table 1 and Supplemental Table 4). The colorless and colorful orbs grow to average diameters of 1.69 cm and 1.66 cm, respectively, when placed in deionized (DI) water, and 1.41 cm and 1.43 cm, respectively, when placed in tap water. Very large colorful orbs resulting from larger dehydrated spheres (∼ 4 mm) are also used in experiments and have an average diameter of 3.87 cm after being placed in tap water (Table 1 and Supplemental Table 4). HydroOrb size is the only physical parameter that is significantly different between orbs (colorless and colorful) made with DI water, orbs made with tap water, and large orbs (Supplemental Table 4).

We soak the HydroOrbs in water for at least 1–4 days before the start of an experiment to ensure maximum hydration (McLafferty et al., 2023). The fully hydrated orbs deform in a linear elastic manner (Dijksman et al., 2017) until they reach a yield point, after which they fracture into smaller pieces (James et al., 2020). The average yield stresses, τ_y, of the orbs are ∼ 15 kPa for the large orbs, between ∼ 72 and ∼ 79 kPa for colorless small orbs soaked in DI and tap water, respectively, ∼ 57 kPa, and ∼ 43 kPa for the colorful small orbs soaked in DI and tap water, respectively. All yield stress calculations show relatively wide standard deviations (Supplemental Table 4). To reduce the average yield stresses and

standard deviations of the orbs, we puncture the HydroOrbs perpendicular to the outer edge of the orbs towards the center with a 24-gauge sewing pin (diameter 0.55 mm). The puncture length to orb diameter ratio is 0.4 for all orb types. The puncture introduces a line of weakness and is needed to penetrate a rind of denser material in the outermost 1–2 mm of the orb (Chang et al., 2018). This line of weakness leads to decreased yield stresses of $\sim$ 25 kPa for the colorless and colorful orbs made with DI water, while the colorless and colorful orbs made with tap water have yield stresses of $\sim$ 21 kPa, and the large orbs have a yield stress of $\sim$ 7 kPa (Table 1). Note that all HydroOrb types have yield stresses that overlap when taking standard deviation into consideration. A comprehensive list of orb physical properties can be found in Supplemental Table 4.

2.2. *Results from Laboratory Shear Experiments*

Laboratory experiments are conducted with both the colorless and colorful HydroOrbs, including the large orbs, for a total of six experiments. Initial experiments were conducted with colorless orbs only. The reason for adding colorful orbs in addition to the colorless ones is that they are better visible in the experiments. The HydroOrbs are punctured before every experiment, and only one type of orb is placed in the ring shear apparatus for each experiment. Experiments CL_D1 and CL_D2 use colorless DI water orbs, while experiment CL_T uses tap water orbs. Experiments CF_D and CF_T are repeats of CL_D2 and CL_T, respectively, but with colorful orbs. Experiment CF_LG uses large colorful orbs. The experiments are conducted at average confining pressures between 2.04 and 2.67 kPa, with the exception of CL_D1 and CF_LG, which are deformed at relatively low confining pressures of 0.82 kPa and 0.89 kPa, respectively. A list of experiments and parameters can be found in Table 1. Each experiment comprises 10–20 rotations of the experimental chamber depending on water leakage out of the ring shear apparatus. Each full rotation takes 330 s due to an imposed angular velocity of 0.019 rad/s (corresponding to an average linear velocity of 0.28 cm/s) at the baseplate of the experimental chamber. During each experiment, we record the horizontal pulling force and the normal force. In addition, HydroOrb migration and failure are recorded throughout the experiments with two cameras. One camera is mounted to the experimental chamber and rotates with the motor documenting deformation in one location of the experiment. The other camera is stationary and positioned at the outside of the annulus facing towards the center, documenting the variability throughout the experiment.

2.2.1 *Orb Rearrangement and Failure*

HydroOrb rearrangement is observed in every experiment regardless of confining pressure. Most orb movement takes place in the top half of the experimental chamber in the form of individual or multiple orbs sliding past each other. The orb movement is most prominent close to the shear boundary beneath the top plate. There is little to no orb rearrangement at the bottom of the experimental chamber, where the orbs move passively with the bottom plate of the chamber. Instead, these orbs show elastic deformation due to stress imparted from orb rearrangement above. Due to rearrangement, we observe HydroOrbs moving both vertically and horizontally within the experimental chamber. After 5–10 rotations, widespread orb rearrangement throughout the height of the experimental chamber lessens and becomes mostly limited to the top half of the chamber as the total volume decreases due to HydroOrb failure.

Table 2

List of physical experiment parameters, including the percent of broken HydroOrbs, the bottom and top height of the fragment band in the material chamber, and the average orb diameter

Experiment	% Orbs broken	Final fragment band location (average height in cm)	Average orb diameter (cm)
CL_D1	0	–	1.69 ± 0.09
CL_D2	16.2	4.5–9	1.69 ± 0.09
CL_T	6.4	5–10.5	1.41 ± 0.06
CF_D	18.9	4–8	1.66 ± 0.08
CF_T	2.7	4–10.5	1.43 ± 0.08
CF_LG	21.1	6–9.5	3.87 ± 0.25

HydroOrb failure is observed in all experiments except for experiment CL_D1 ($\tau_y = 25.44$ kPa, for standard deviations, see Table 1) which was conducted at a lower confining pressure (0.82 kPa). However, the percentage of broken orbs differs between experiments (Table 2), with the highest percentage of broken orbs in experiment CF_LG ($\tau_y = 7.07$ kPa), even at a low confining pressure (0.89 kPa), and the lowest percentage of broken orbs in experiment CF_T using colorful tap water orbs ($\tau_y = 21.97$ kPa) despite a larger confining pressure (2.20 kPa). Broken orb percentage is larger in the experiments using DI water orbs compared to tap water orb $\tau_y = 21.43$ experiments, regardless of whether the orbs are colorful ($\tau_y = 25.62$ kPa for DI and $\tau_y = 21.97$ kPa for tap water orbs) or colorless ($\tau_y = 25.44$ kPa for DI and $\tau_y = 21.43$ kPa for tap water orbs).

During an experiment we observe downward orb fragment migration from the shear boundary at the top of the experimental chamber towards the middle of the chamber, where the fragments fill the voids between unbroken HydroOrbs. However, fragments do not migrate all the way to the bottom of the material chamber; instead, they stop a few centimeters above the bottom plate to create a band of fragments in the middle of the experimental chamber (Fig. 1). The thickness of the fragment band increases throughout the experiment as more orbs break at the top of the chamber. The band of fragments reaches a finite thickness during an experiment after HydroOrb failure stops and fragments are no longer supplied from the shear boundary. Once the supply of fragments stops, the thickness of the fragment band decreases as the fragments consolidate (Fig. 1). This consolidation happens in experiments CL_D2, CF_D, and CF_LG after orbs are no longer observed to fail at the shear boundary. The fragment band formation and consolidation are less apparent in experiments CL_T and CF_T where smaller tap water orbs are used. Table 2 summarizes the final fragment band location and thickness for each experiment. Notably, fragment band thickness decreases with increasing orb size used in the experiment (Table 2). For example, experiments involving small tap water HydroOrbs (Fig. 2c and e) result in a fragment band thickness of 5.5–6.5 cm (CL_T and CF_T, respectively), whereas experiments with DI orbs (Fig. 2b and d) result in fragment band thickness of 4–4.5 cm (CF_D and CL_D2, respectively). CF_LG (Fig. 2f) results in the thinnest band of fragments at 3.5 cm (Table 2). The reason could be that fragment formation slows down or stops around rotations 7–10 for the large and DI orbs so no more fragments are supplied from the top. The fragment band then compacts due to orb movement at the top, pushing the fragments downward while the bottom of the fragment band stays at the same height (due to no orb rearrangement below).

2.2.2 *Force Measurements*

The pulling force magnitude and its variance calculated from experiments mirror the observations of orb rearrangement and failure discussed above. Orb rearrangement is recorded in the force data as large force magnitude oscillations at different frequencies and amplitudes due to the spring boundary condition. These large force oscillations result in relatively greater variance values. Where orb rearrangement is most prevalent at the beginning of the experiments, the pulling force magnitude and variance are at (or close to) their maximum in most experiments (Fig. 3). The pulling force and variance values decrease in magnitude with increasing rotations as HydroOrbs fail. The only exception to the decrease in force magnitude and variance through increasing rotations is CL_D1, where there is orb rearrangement but no orb failure in the presence of a relatively low applied normal force. In CL_D1, the force magnitude and variance values are less than the values from experiments where the applied normal force is greater (Fig. 3).

Most experiments have maximum force magnitudes and variance values in the first rotation. After the first rotation, the force magnitude and variance significantly decrease. Conversely, the last several force magnitude and variance values for each experiment are relatively constant (Fig. 3). To describe the relationship between force magnitude or variance with increasing strain, we fit power law trendlines to the data for all experiments to help guide the eye and make the pattern in the data more visible (Fig. 3). Conversely, where there is no orb failure in CL_D1,

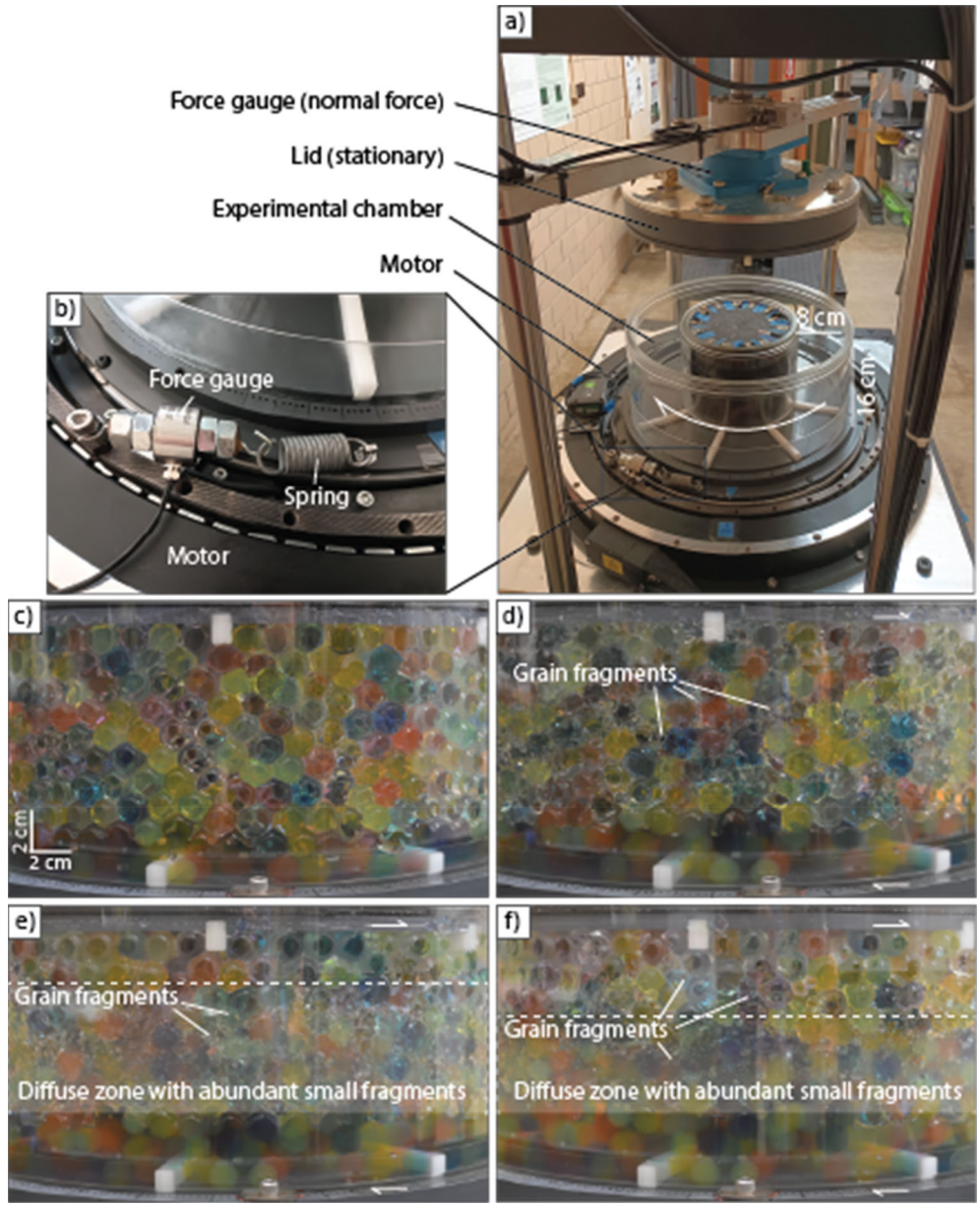

Figure 1

a Photograph of the experimental setup with a close-up of the spring/force gauge assembly in **b**. **c**–**f** Photos of experiment CF_D taken from the outside of the experimental chamber looking towards the smaller cylinder at the center. **c** HydroOrbs before the experiment, **d** after rotation 5, **e** after rotation 10, and **f** after the final rotation. Transparent white box indicates zone with abundant small fragments. Few individual larger fragments are indicated. Note the decrease in height of the fragment band between rotation 10 (**e**) and after the final rotation (**f**); no fragment band has formed yet in **d**

there is no decrease in force magnitude and variance values with increasing strain resulting in the poor power law trendline fit.

While the average pulling force magnitudes for different experiments yield different trendlines, the error bars on individual force magnitude points overlap heavily between experiments. In addition,

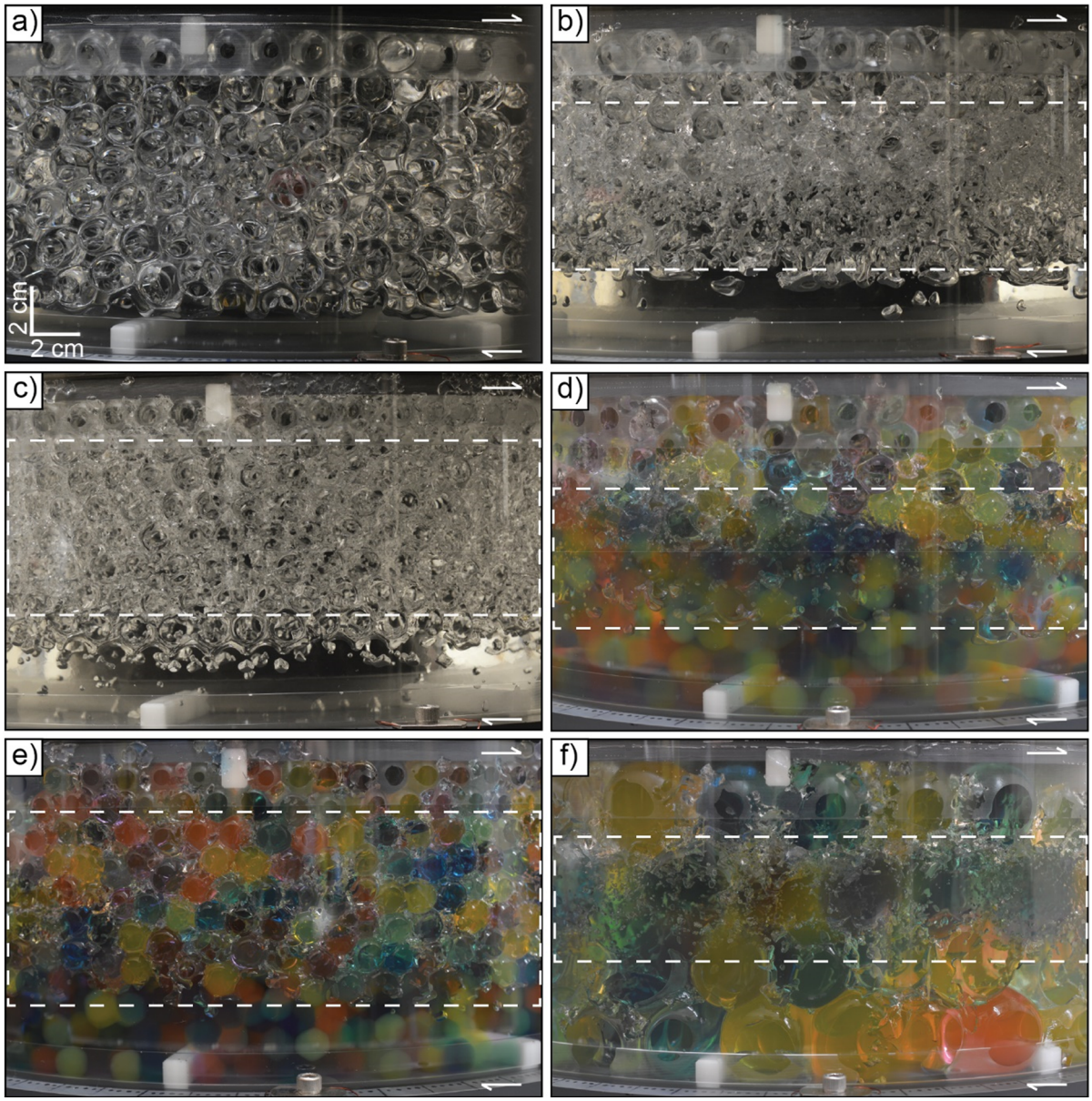

Figure 2
Photos of the physical experiments after the last rotation, taken from the outside of the material chamber looking toward the inner cylinder. **a** CL_D1, **b** CL_D2, **c** CL_T, **d** CF_D, **e** CF_T, and **f** CF_LG. Fragment band location noted with dashed box. Note the absence of fragment band in **a** due to the absence of fracturing

individual variance points overlap between experiments, making it difficult to determine differences (if there are any) in material deformation between the experiments. According to the power law trend, both experiments involving the smallest orbs, CL_T and CF_T, record the largest variance values towards the end of the experiments. Experiments CL_D2 and CF_D record comparable variance values, which are less than those from the tap water orb experiments. The experiment with the largest orbs, CF_LG, records the smallest variance values (except CL_D1) towards the end of the experiment. As

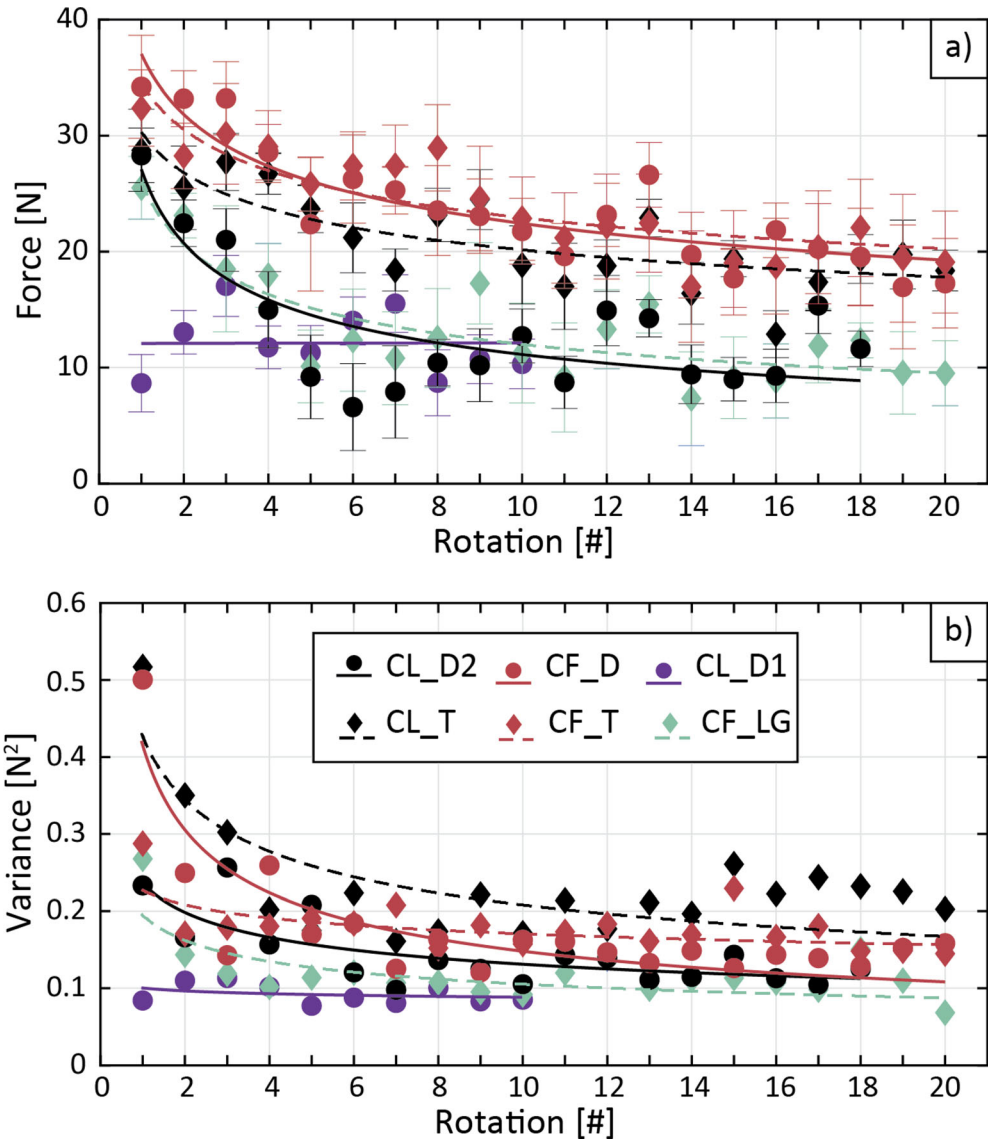

Figure 3
Force data results for the experiments with power law trendlines. **a** Pulling force magnitude with increasing rotations, **b** variance. Note each rotation is completed in 330 s. CL-D1 failed after ten rotations. Data are from McLafferty et al. (2023)

HydroOrb size increases, variance at the end of the experiment decreases, which is consistent with less orb rearrangement due to grain failure at the beginning of the experiment. The experiment with the most orb failure is experiment CF_LG (21.1%), which records the lowest variance values at the end. Further, 16.2% of orbs failed in experiment CL_D2, and 18.9% failed in experiment CF_D, corresponding to similarly low variance values towards the end of the experiments.

2.3. *Summary of Laboratory Shear Experiments*

Most orb rearrangement and fragment formation (when present in experiments) take place near the top of the experimental chamber. Throughout the experiment, the orb fragments migrate downward to the

middle of the experimental chamber to form a fragment band. This brittle failure of the HydroOrbs is recorded in the force gauge data as a decrease in force magnitude and variance. When no orb failure is present (experiment CL_D1) there is little to no decrease in force magnitude and variance.

The confining pressures of most experiments fall within the range of 2.0–2.2 kPa and result in no systematic difference in orb failure, force magnitude or variance. However, when considering only one HydroOrb type (such as orbs made with DI water), the confining pressure does play an important role in grain failure, with the lower confining pressure in CL_D1 resulting in no orb failure. As confining pressure increases within the three experiments with DI HydroOrbs, the percentage of broken orbs (Table 2) and pulling force (Fig. 3a) also increase. Alternatively, experiment CF_LG is conducted with a similarly low confining pressure to CL_D1 ($\sim$ 0.9 and $\sim$ 0.8 kPa, respectively) but results in the highest percentage of orb failure across all experiments. Therefore, when confining pressure is held relatively constant, the orb properties, such as diameter and yield stress, dictate orb failure.

Combining both the visual results and force data from the analog experiments allows us to correlate HydroOrb size and grain comminution. As orb size increases, the percentage of broken orbs also increases, regardless of confining pressure. The fragment band thickness and the force magnitude and variance are also correlated with the size of HydroOrbs. Fragment band width recorded at the end of the experiments decreases with increasing orb size. Finally, the force and variance magnitudes at the end of the experiments are anti-correlated to orb size.

3. Numerical Experiments

Numerically, granular media are most often studied by employing the Discrete Element or Lattice Solid methods (Abe et al., 2004; Cundall & Strack, 1979; Mora & Place, 1993, 1994; Place & Mora, 1999; Wang et al., 2006). Both methods simulate systems as an assemblage of discrete particles interacting with each other allowing the tracking of mechanical interactions between particles. There are two common approaches when simulating a granular medium under shear, either as unbonded microparticles (e.g., Mair & Hazzard, 2007; Morgan & Boettcher, 1999; Rathbun et al., 2013) or as bonded assemblages of microparticles, that act as a singular grain (e.g., Abe et al., 2002; Mair & Abe, 2008; Mora & Place, 1998). In both cases, the interactions between the unbonded particles or the bonded grains are governed by frictional laws and elastic interactions by using equations of motion and simplified force–displacement interaction laws (Wang et al., 2006). Here we are using bonded grains to simulate the HydroOrbs, which allows us to monitor fracturing processes and resulting grain fragment mobility.

3.1. Numerical Setup and Material Parameters

To investigate failure and grain comminution in our models, we make use of the parallel DEM package ESyS-Particle (Abe et al., 2004; Wang et al., 2006; https://launchpad.net/esys-particle). The numerical solution of particle interactions involves computing the net force acting on each particle at a given time, then updating particle velocities and positions via an explicit finite difference integration scheme. The Discrete Element (DE)-particles can be bonded together elastically, thus creating bonded macro-particles, which act as a representation of the HydroOrbs in the physical experiments. The breaking of bonded grains results in unbonded (micro-)particles. These unbonded particles can interact with other unbonded microparticles or with bonded grains via frictional forces. Henceforth, we will refer to grains made of many small particles as (bonded) grains and to the individual unbonded small particles as microparticles.

The geometry of the numerical simulations resembles the analog ring shear apparatus (see Table 3 for a comparison between the physical and DEM model dimensions and material parameters). Two unbreakable indented plates encompass the numerical grains (Fig. 4a). The size of the grooves on the plates (10 mm height) matches the laboratory setup, as does the distance between the plates (140 mm). The interstitial space between the plates is filled with non-overlapping spheres to represent individual grains (or orbs). The DEM model

Table 3

Dimensions, material properties and boundary conditions of analog and numerical experiments

	Dimensions				Materials							Boundary conditions				
	Length (cm)	Height (cm)	Width (cm)	Grain diameter (cm)	DEM radius (cm)	Density (kg/m^3)	ν^a	φ^b	Y^c (kPa)	$\sigma_y{}^d$ (kPa)	Co^e (kPa)	μ^f	$F_n{}^g$ (N)	$v_s{}^h$ (cm/s)	Spring constant (N/m)	Time step (s)	Exp. time (s)
Analog	94.25[i]	12.6–13	8	~ 1.7	–	~ 1	0.39 ± 0.07	–	107–137	25	–	–	60–161	0.28	9712	1	3300–6600 (10–20 rotations)
DEM	14	14	8	~ 2.0	0.05–0.2	1e6[j]	0.4	45°	135	–	30	0.05	8–50	0.3	-	1e-3	950

[a]Poisson ratio; [b]Friction angle; [c]Young's modulus; [d]Yield stress; [e]Cohesion; [f]Coefficient of friction; [g]Normal force; [h]Shearing velocity; [i]Circumference of the experimental chamber (or the average distance rotated for one full rotation); [j]High-density/mass approximation (see Sect. 4 for details)

represents the plates and grains as assemblies of discrete, spherical microparticles bound to oneanother via elastic-brittle beam interactions. A geometry construction library (called GenGeo), provided as part of ESyS-Particle, is used to generate these bonded microparticle assemblies. GenGeo implements a random, space-filling sphere packing algorithm as described by Place and Mora (2001). The algorithm fills a specified three-dimensional volume with non-overlapping spheres whose radii are constrained to a specified range of sizes (0.5–2.0 mm). The algorithm generates ca. 30,000 microparticles for each of the grooved plates and ~ 900 microparticles for every one of the 116 interstitial grains (Fig. 4b, inset). The number of grains is not specified as the GenGeo library is also used to fill the space between the plates with large spheres of ~ 2 cm diameter, which are thereafter replaced with assemblies of microparticles. Once the microparticle assemblies have been generated, the GenGeo library identifies all pairs of microparticles that are touching one-another, producing a list of ca. 320,000 bonded interactions. The size distribution of the microparticles is not specified although tests confirm that this approximates a power-law with a fractal dimension close to 3; an expected result given that GenGeo employs a space-filling generative algorithm. The choice of minimum and maximum microparticle radii for the packing algorithm was based upon experience by authors employing ESyS-Particle for similar shear-induced fragmentation studies (e.g., Abe & Mair, 2005, 2009; Mair & Abe, 2011) to ensure that the macroscopic mechanical properties of each grain are statistically similar and that the resultant micro-scale surface roughness does not yield an unrealistically high bulk friction coefficient. A comparison of the shear forces acting on the plates during simulations with experimental measurements verifies that the selected geometrical parameters yield realistic macroscopic response.

Bonded microparticle pairs undergo elastic-brittle interactions that account for normal, shear, bending and torsional deformation. A bond failure threshold is defined by the Mohr–Coulomb criterion. A bond will fail (or break) if the shear stress within the bond exceeds its shear strength

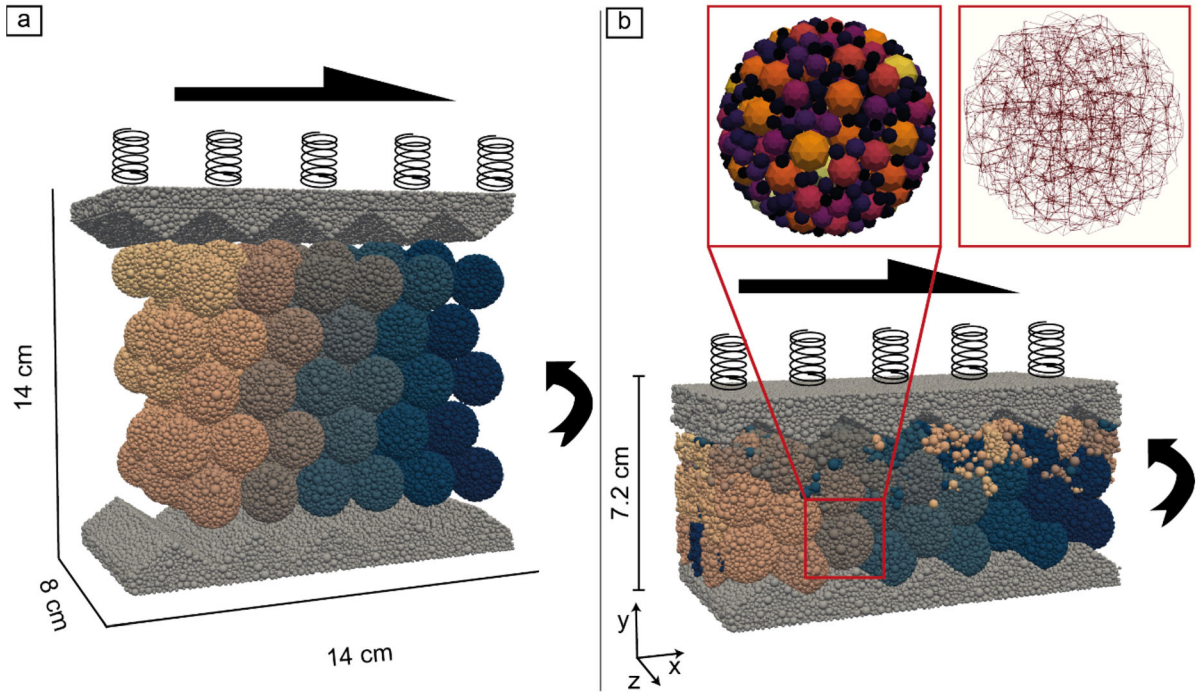

Figure 4
Geometry and boundary conditions of the DEM models. Colors on the brown to blue color map shows microparticles that form one bonded grain. Vertical springs denote constant force applied on the moving plate, horizontal arrows correspond the shearing velocity implemented on the moving plate, curved arrow denotes periodic boundary condition along the YZ-plane. **a** Initial geometry of the numerical models. **b** Geometry at the end of the simulation; insets show one bonded particle, composed of ca. 900 microparticles (left), elastic bonds between individual microparticles (right). The black to orange color scale shows micro-particle radii within one bonded grain. Normal force in this model is 38 N. Note the different vertical size of the model in the first step (14 cm; **a**) versus the final step (ca. 7.2 cm; **b**)

$$\tau_y = C + \sigma_n tan\varphi_f$$

where C is the cohesive strength of the bond for zero normal stress (σ_n) and φ_f is the internal angle of friction of the bond (Table 3). Wang et al (2006) provide a comprehensive mathematical treatment of the bonded particle interactions utilized by the simulations conducted herein. The internal angle of friction for individual bonded microparticle interactions has only a minor influence on the strength and the macroscopic (bulk) friction angle of an assembly of bonded microparticles. Consequently, it is typical to set the internal angle of friction to 45° and tune the cohesive strength instead.

When the bond failure threshold of a bonded microparticle pair within a grain is reached, the bond breaks and the two microparticles become unbonded. Thereafter, these unbonded microparticles undergo elastic repulsive frictional interactions should they contact one another or other microparticles to which they are not bound. These interactions are characterized by a coefficient of friction, a Young's modulus, and the Poisson's ratio. Dimensions and material parameters of the bonded grains are chosen to mimic the HydroOrbs (Table 3).

Simulating the full experimental domain would be computationally very expensive; we, therefore, simulate a small section of the domain and use periodic boundary conditions on the left and right vertical boundaries; thus, particles moving out on one side of the domain appear on the other side, without any loss of bonds, velocity, etc. The numerical simulations are characterized by three distinct phases. The first one is the compaction of the grains, achieved by applying constant normal force on one plate (spring in Fig. 4). This phase starts at the beginning of the simulation, and normal force is kept constant throughout the simulation. Note that instead of using the same

normal force values as in the experiment, we use values that correspond to the same normal stress; since our numerical domain is smaller than the experimental chamber, the numerical normal forces are also smaller (Table 3). Once the grains have been sufficiently compacted and a steady state is achieved, a constant shearing velocity is applied on the top plate under the same constant normal force. This phase starts at time t = 250 s, and the shearing velocity increases linearly from zero to a steady velocity at t = 350 s. In the third stage, the shearing velocity is kept constant until the end of the simulation (t $\sim$ 950 s). Moreover, the model has frictionless walls front and back (XY-plane). The presented numerical models mimic the setup and material parameters of the physical experiments with the DI water HydroOrbs (CL_D1, CL_D2, and CF_D), which mainly differ in normal force. A detailed comparison between the experimental and numerical boundary conditions is given in Sect. 4.1. We complement these numerical models with five additional ones in order to investigate a wider normal force distribution (Table 3). The purpose of the numerical models is to evaluate the effect of normal force on grain comminution and provide data on parameters that cannot be measured in the analog experiments, such as the rate of breaking of bonds during shearing.

We vary the normal force from 8 to 50 N, at 6 N increments, while using a very low coefficient of friction ($\mu = 0.05$) to account for the slippery surface of the HydroOrbs forming due to the thin water film that surrounds them. Since we have no measure of the cohesion of the HydroOrbs, we use a value close to the measured yield stress of the HydroOrbs (Tables 1 and 3).

3.2. Numerical Results

3.2.1 Grain Rearrangement and Failure

Grain rearrangement is observed in all the numerical experiments, regardless of normal force, similarly to the laboratory experiments. Moreover, most grain movement happens at higher normal forces, and tends to localize along the moving plate, which is where normal force and shearing velocity are applied. At low normal forces (Fig. 5a, b), fewer grains break, leading to fewer microparticles, which are mainly located in the upper third of the domain, close to the moving plate. As normal force increases, however, the number of broken grains increases as well (Fig. 5c, d). Notably, microparticles travel until about the middle of the model (Fig. 5c, d top). Finally, vertical velocities increase with normal force (Fig. 5c, d bottom) close to the boundary with the moving plate. Given the absence of gravity in our numerical models and the fact that compression is applied at the top, the grains are more mobile close to the moving plate, while the grains closer to the fixed plate are jammed.

Figure 6a shows the number of elastic bonds between microparticles that break during the simulation. All experiments, independent of applied normal force, show a distinct change in slope in the number of broken bonds some tens of seconds after the simulation starts. This change reflects the moment the moving plate touches the grains. A second change in slope at round $t = 100$ s denotes the moment when the bonded grains, squeezed by the moving plate, finally touch the fixed plate. The third change in slope occurs between $t = 250$ s (first vertical dotted line in Figs. 6a and 7a) and $t = 350s$ (second vertical dotted line in Figs. 6a and 7a), which is the time interval between the onset of horizontal shearing at the moving plate and the moment velocity reaches its maximum value (velocity is increased linearly during these 100 s). During the first two stages (compaction), the amount of broken bonds is significantly smaller than during shearing. In the final stage, the number of broken bonds slowly approaches the x-axis asymptotically. With increasing normal force, the amount of broken bonds increases. The rate of bond breaking versus shear strain (Fig. 6b) shows that most of the fracturing occurs at the initial stages of shearing and that bond breaking reaches a steady state after the first 5 full rotations (shear strain is equal to 5). Finally, bond breakage is higher at higher normal forces, while the dataset for all normal forces shows episodic spikes in breaking rate.

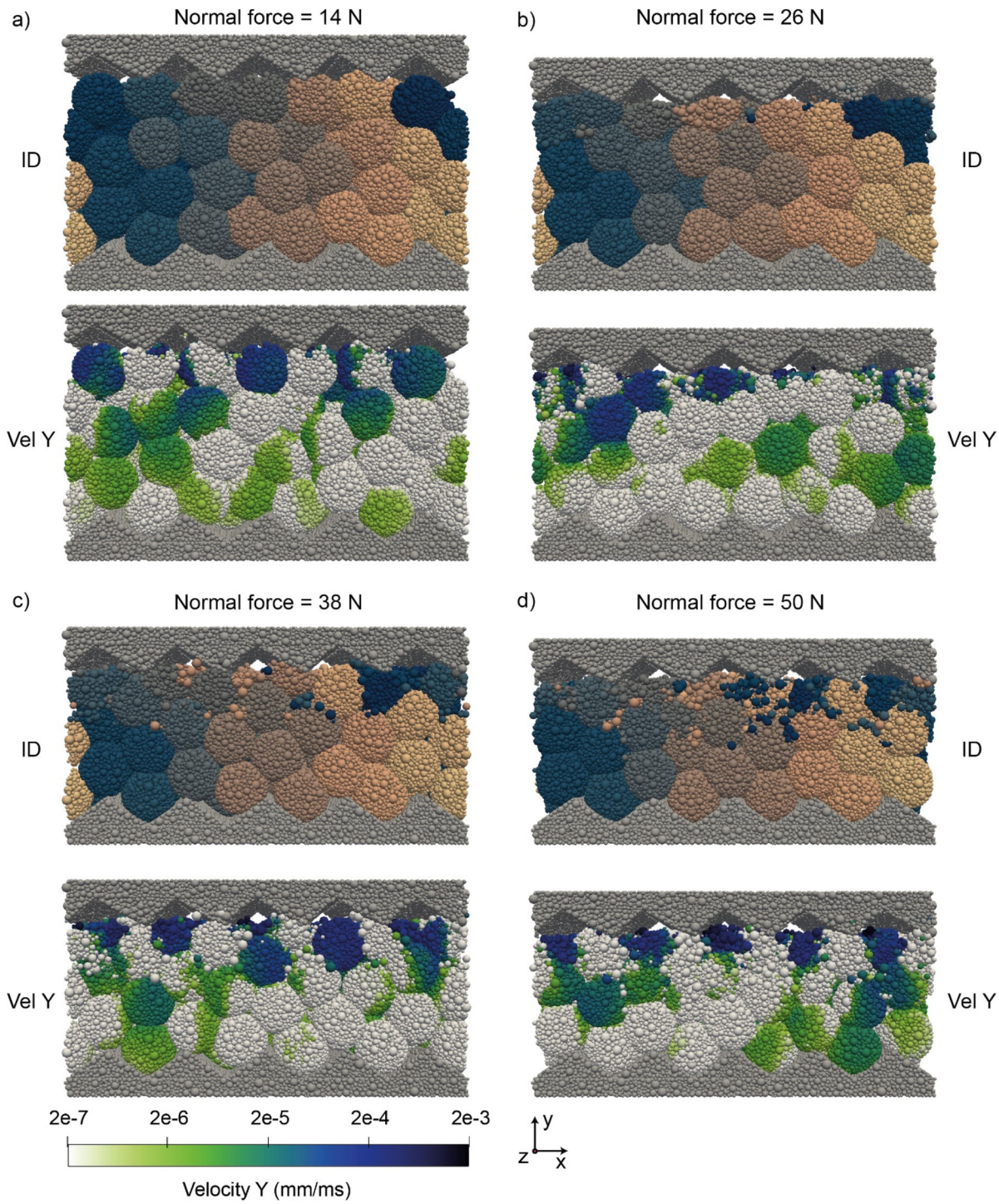

3.2.2 *Force Measurements*

We measure horizontal force of the models at the fixed plate. Due to the absence of shearing during the initial compaction stage, the horizontal force at the fixed boundary is zero at the beginning of each experiment (Fig. 7a). The second compaction phase is shown by the low-amplitude variation of the

◀Figure 5
Particle ID's (top of each panel) and vertical velocity (bottom of each panel) for models with varying normal force (14–50 N) at the end of each simulation. With increasing normal force, more microparticles are extracted from their parent grains (ID panels—top). These microparticles are then transported from the moving plate toward the center of the domain. Vertical velocity is the highest close to the moving plate, and it decreases towards the fixed plate. With increasing normal force, the vertical velocity increases with the highest values close to the moving plate. For a visualization of the broken grains only, see Fig. 10 in the Appendix)

horizontal force (left of the first vertical dotted line), while the onset of shearing is clearly visible between 250 and 350 s (between the dotted vertical lines). An increase in the normal force of the model translates to an increase in the horizontal force. In all models, maximum force values are observed after the onset of shearing (Fig. 7a, first vertical line), while after constant shearing is achieved, the horizontal force significantly decreases particularly for lower normal forces. At higher normal forces, the variation in the horizontal force is also larger (Fig. 7a after the second dotted vertical line).

Grain rearrangement and failure are presented in the horizontal force data as force oscillations at different frequencies and amplitudes throughout the simulation. These force oscillations are larger for higher normal forces (Fig. 7a), which result in relatively greater variance values (Fig. 7b). Notably, variance values are larger when calculated using force data from the onset of shearing (first dotted vertical line in Fig. 7a), compared to the variance calculated after full shearing velocity has been achieved (second dotted vertical line in Fig. 7a). This agrees with our observations that most of the bond breakage occurs during the initial stages of shearing (Fig. 6a, b).

Finally, to assess the effect of normal force on the overall behavior of the numerical models, we plot the percentage of broken bonds (Fig. 8; black circles) and the maximum recorded horizontal force (Fig. 8; cyan circles) of each model. Increasing normal force results in higher amounts of broken bonds; this, in turn, results in more fracturing of the grains. In the highest normal force model (50 N), we observe the highest percentage of broken bonds ($\sim$ 12%). Notably, the models with the highest bond breakage and highest horizontal force are also the ones with the largest variance of the horizontal force (Fig. 7b).

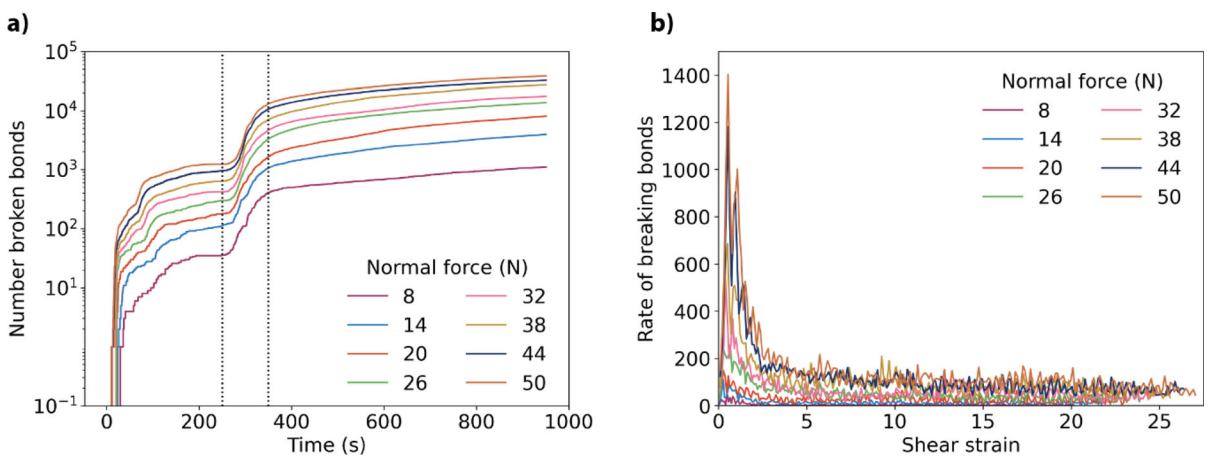

Figure 6
a Number of micro-particle bonds breaking with time for models with varying normal forces. Y-axis is in logarithmic scale. The dotted lines represent the moment when shearing velocity is applied (first line) and the time when maximum shearing velocity has been achieved (second line). **b** Rate of bond breaking with shear strain for models with varying normal force. Legend in b shows the normal force for each model (in N) and is the same in both panels

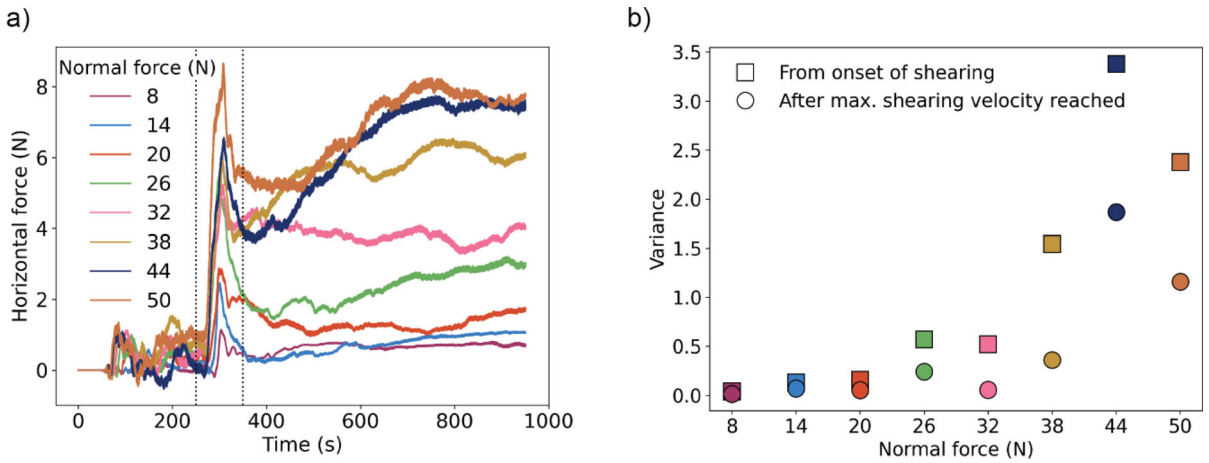

Figure 7
a Horizontal force (in N) measured at the fixed plate, and **b** variance of the measured horizontal force at the onset of shearing (square) and after full shearing velocity has been achieved (circles) for models with varying normal force. The dotted lines represent the time when shearing velocity is applied (first line), and the time when maximum shearing velocity has been achieved (second line). Legend in **a** shows the normal force used for each model (in N) and is the same for both panels

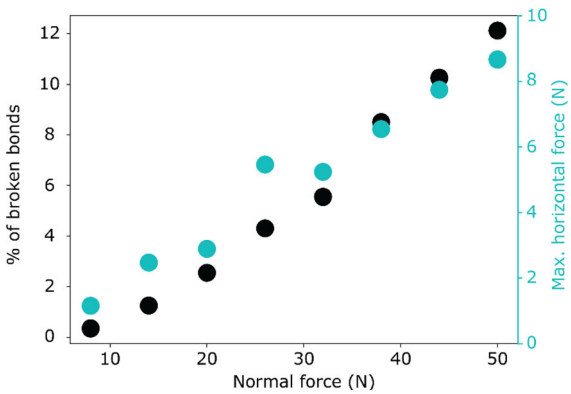

Figure 8
Percentage of broken bonds (black circles; left vertical axis) and maximum recorded horizontal force in N (cyan circles; right vertical axis) for models with different normal forces (x-axis). The number of interparticle bonds at the beginning of each simulation is ca. 320,000

4. Discussion

4.1. Experiments Versus Numerical Models—Limitations

The first difference between the two approaches is the fact that the numerical domain does not take the curvature or the varying shear rate between the inner and outer rings of the experiment into account. Moreover, the laboratory setup has an elastic element between the motor and the force gauge, which is lacking in the numerical setup. Having an elastic element in the experimental boundary condition allows for stick–slip motion to occur. Adding such a spring to the boundary condition of the numerical simulation would have increased the complexity of the system and thus would make the interpretation of the results more difficult. However, the indented plates have an elastic component, given by the Young's modulus of the microparticles forming the plates (which is the same as that of the microparticles forming the grains), while we ensure that the plates remain unbreakable by using an increased cohesion (25 times that of the microparticles forming the grains).

The indentations of the numerical plates have the same height as those in the laboratory experiments, but their shape differs. However, the chosen elongated pyramid shape for the numerical models has been used in previous simulations (e.g., Abe & Mair, 2009; Mair & Abe, 2011; Rathbun et al., 2013). Nonetheless, previous studies showed that the shape and size of the rigid plate indentations (roughness) play a role in the grain comminution (Mair & Abe, 2011), the critical displacement (Abe et al., 2002), and mechanical coupling (Rathbun et al., 2013). Therefore, future work would include a more detailed

study on how the shape of the indentations affects our numerical results.

In the experiments, normal force and shearing are applied at different boundaries of the apparatus, while horizontal force is measured at the moving boundary. Nonetheless, because of gravity and the fact that the walls of the experimental chamber are moving with the bottom boundary, deformation localizes at the stationary boundary in the analog experiments (top). In the numerical models, we impose both normal force and shearing at the same (moving) plate, while we measure the horizontal forces at the fixed plate, away from the shear zone, like in the experiments. This overall shearing behavior is common both in laboratory experiments of granular shear at low stress and high strain rates (e.g., Bocquet et al., 2001; Losert et al., 2000; Mueth et al., 2000; Pouliquen & Gutfraind, 1996; Veje et al., 1999), as well as in 2D (Aharonov & Sparks, 2002) and 3D numerical models (Mair & Hazzard, 2007; Rathbun et al., 2013).

Another difference between the experimental and the numerical setup is the high-mass/density approximation used in the numerical models. Because the minimum stable numerical time step depends on particle density, a very small density, such as that of the HydroOrbs, would result in a very small stable time step, which in turn would make the numerical computation too expensive (see also Appendix sect. "(6.2)"). This is a common issue in the DEM, and one way to counter it is by using much higher densities (several orders of magnitudes larger). However, larger densities generally result in inaccurate accelerations. Thus, for the high-mass approximation to not influence the overall deformation, a penalty factor is introduced (a dampening of the particle kinetic energy; Cundall & Strack, 1979). This factor causes the right-hand-side of the equation $F = ma$ to approach zero. In principle, we are approximately solving the remaining $F = 0$ differential equation, i.e., the steady-state solution of the system of equations comprising the DEM simulation. Because the density is not infinite (accelerations do not equal zero), the DEM solution will be "quasi"-static rather than steady-state. Since the laboratory experiments were conducted under quasi-static conditions, by employing the high-mass approximation with the penalty factor, we maintain realistic deformation rates in the model. The use of this approximation is further facilitated by the absence of gravity since a very large density would result in very large acceleration. Therefore, in combination with the absence of gravity and an artificial dampening of the kinetic energy of the particles, this approach allows for faster computations.

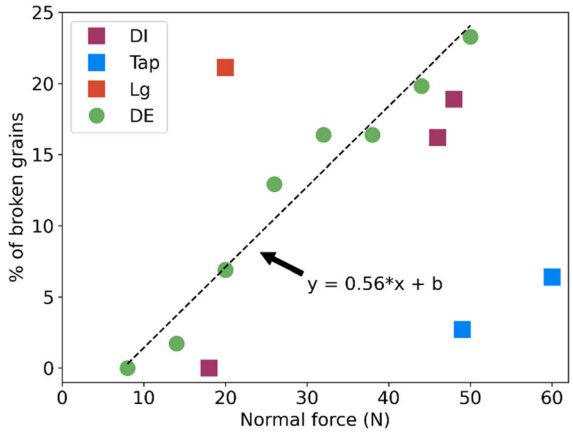

Figure 9
Percentage of broken grains with increasing normal force in analog (squares) and numerical models (circles). The slope of the curve y = ax + b is a = 0.56, where x is the normal force and y is the percentage of broken grains. *DI* orbs immersed in de-ionized water, *Tap* orbs immersed in tap water, *Lg* large orbs immersed in tap water, *DE* discrete element grains

4.2. Grain Rearrangement and Failure

To compare the results between the analog and numerical experiments, we plot the percentage of broken grains observed in each model versus the equivalent normal stress (Fig. 9). Not surprisingly, an increase in normal force results in an increase in the number of grains that break in both approaches. The small discrepancy between the percentage of broken bonds (Fig. 8a) and the percentage of broken grains in the numerical models (Fig. 9) can be attributed to the fact that a single bond breaking from a grain results in this grain being considered broken. Since there are multiple orders of magnitude fewer grains than bonds (116 versus $\sim$ 320,000), this leads to higher percentages of broken grains. To dampen this effect, we arbitrarily consider a grain broken after it has lost 10% of its mass.

We can fit the results of the broken grains with the normal force of the numerical models (Fig. 9, circles) using a linear regression of the form $y = ax + b$, where y is the percentage of broken grains, $a = 0.53$ and x is the normal force. Because the numerical models are calibrated based on the dimensions and materials parameters of the DI experiments, we exclude all the other experiments from the comparison (blue and orange squares, respectively). We interpret the difference in the results of the excluded models to reflect the effect of grain size. The physical experiments show that with an increase in orb size, the percentage of broken orbs also increases regardless of normal force. This observation is in line with previous findings showing that grain size plays an important role in the macroscopic behavior of a fault gouge (e.g., Anthony & Marone, 2005). One potential explanation for the different behavior of the smaller HydroOrbs is that smaller HydroOrbs made with tap water may be able to rearrange and roll or slide past other orbs to fit into void spaces more readily than larger orbs such as those made with DI water and the large colorful orbs.

In the physical experiments, migration of orb fragments is observed from the top of the model, where shearing is imposed, towards the middle of the experimental chamber. Typically, the orb fragments stop a few centimeters above the bottom plate, where they create a band of fragments in the middle of the experimental chamber (Figs. 1 and 2, Table 2). The thickness of the fragment band increases throughout the experiment as more orbs break at the top of the chamber and then decreases when the fragment supply from near the top of the experiment stops. Throughout the numerical models, we observe bond breakage and then migration of the unbound microparticles from the moving plate/shear boundary toward the middle of the model domain. Similarly to the physical experiments, the numerical microparticles move away from the shear zone towards the middle of the model domain (Figs. 5b–d and 10). Experiments on sheared mixed grain sizes have shown both the migration of smaller particles away from the shear zone and towards the shear zone (e.g., Fan & Hill, 2011; Gray & Thornton, 2005; May et al., 2010; Stephens & Bridgwater, 1978). One mechanism that can explain the motion of the small particles in our experiments is kinetic sieving. During kinetic sieving, smaller grains move downward by falling into pores opened by the rearrangement of larger particles, leaving larger grains preferentially on top (Fan & Hill, 2011; Gray & Thornton, 2005). Downward fragment migration may therefore halt when no voids are opened from the movement of the large intact grains (little orb movement at the boundary far from the shear zone in the experiments). This mechanism does, however, not explain the motion of the grains in the numerical results because gravity is the driving force for kinetic sieving, and all our numerical simulations are performed in the absence of gravity. Siman-Tov and Brodsky (2018) suggest that grain segregation, where smaller grains accumulate in layers away from the shear boundary and model edges, can be controlled by shear gradients. This mechanism does not rely on gravity as a driving force. Instead, smaller particles migrate away from the high shear rate regions and accumulate in low-shear rate regions and larger/unbroken orbs move towards the area of the highest shear strain (Fan & Hill, 2011; Stephens & Bridgwater, 1978). Note that the experiments by Siman-Tov and Brodsky (2018) have been conducted at high shear rates. If a similar process is at play at the strain rates used in the presented numerical simulations remains to be investigated.

One advantage of the benchmarked numerical models is that we can gain insight into the rate of bond (and hence grain) breakage with time and shear (Fig. 6), which is not possible to measure in laboratory experiments. The numerical results suggest that bond (grain) breakage occurs in episodic pulses (large spikes in Fig. 6b), which denote temporal clustering of comminution events (Mair & Abe, 2008). The rate at which bonds break becomes significantly smaller after a shear strain of 1–3. Additionally, the comminution rate is low for low normal forces and increases with higher normal forces. Previous studies corroborate the dependency of comminution rate on normal force and the gradual decrease in bond breakage rate with accumulated strain (Abe & Mair, 2005; Mair & Abe, 2008). In DEM models by Mair and Abe (2008), the largest spikes in bond breakage rate decrease significantly after a strain of 1, which coincides with the approximate strain at which the

macroscopic friction in their models reaches steady state. However, in their models, compaction is the main reason for bond breakage, while in our models, compaction is responsible for only a small portion of bond breakage (see also Fig. 11 in the Appendix), while grain rearrangement and shearing are the driving mechanisms in our models.

Finally, in the presence of a rough wall (plate indentations), the strength of a gouge is primarily controlled by the friction of the grains, while the contrast of the properties between walls and gouge is insignificant (Rathbun et al., 2013). With increasing particle friction, the overall strength of the gouge also increases (Rathbun et al., 2013). Given the low friction of the grains of the physical and numerical experiments, our models correspond to a weak gouge. Additionally, friction controls the type of motion of particles (e.g., rolling vs. sliding). Particles with high friction move by rolling, while particles with low friction prefer a combination of rolling, sliding, and distribution of shear (Makedonska et al., 2011). Even though we do not investigate the type of movement in the DEM particles, we believe that they also deform via a combination of rolling, sliding, and shearing since the grains in the numerical models and the experiments have a very low friction.

4.3. *Effect of Normal Force*

In both physical and numerical simulations, we observe an increase in broken bonds with increasing normal force. These results agree with the observations by Abe and Mair (2005) and Mair and Abe (2008), who report an increase in fracturing with increasing normal force during their 3D numerical simulations. Additionally, the maximum recorded horizontal force increases (Figs. 7a and 8) with an increase in normal force. The observed force fluctuation with time (Fig. 7a) is smaller for models with a low normal force. This potentially indicates that the granular system flows continuously, since it is unable to sustain the applied shear stress (Arcangelis et al., 2011). In the numerical simulations, peak horizontal forces (Fig. 7a) coincide with the steepest curve in the broken bond curves (Fig. 6a), while post-peak forces fluctuate and the rate of breaking of bonds is almost constant (Fig. 6b). The dramatic drop in horizontal force corresponds mainly to grain fracturing while post-peak fluctuations reflect increased grain rearrangement. The same behavior can be observed in the physical experiments, where breaking of the orbs leads to a decrease in variance and total force (Fig. 3). Most orb failure occurs toward the beginning of the analog experiments where the steepest decrease in pulling force and variance are observed (Fig. 3). In the numerical experiments the maximum rate of bond breakage indicating orb failure also occurs at the beginning of shearing (Fig. 6b).

The variance (average fluctuation of the pulling force) in the physical experiments reaches a relatively steady value after the initial drop in every experiment. In contrast, where no orb failure occurs (experiment CL_D1), the total force and variance values are relatively constant throughout the experiment while recording only orb rearrangement. These observations agree with Wu et al. (2022), who found that in post-peak stress-displacement curves, a dramatic stress drop is due to rock fragment crushing, and the moderate decline indicates grain rotation. The variance of the horizontal force in the numerical experiments is higher for high values of normal force; this suggests an increased bond and grain breakage for those models.

5. *Conclusions*

We introduced a new elasto-plastic material, HydroOrbs, that has the ability to fracture and can be used to investigate grain comminution in granular media under simple shear conditions. Physical experiments using HydroOrbs showed a clear dependency of grain comminution on normal force when experimenting with orbs of the same size, as well as on grain size when normal force is kept relatively constant. We use these physical experiments to benchmark DEM models of elasto-plastic grains that can move, rotate, and fracture under simple shear conditions. The DEM models are able to qualitatively reproduce both grain comminution and horizontal force fluctuations observed during the physical experiments. The successful reproduction of the experimental results with the DEM formulation will

allow for the use of these numerical models to investigate parameter spaces that are inaccessible for experiments, such as the impact of internal friction and cohesion on the deformation of granular systems.

Acknowledgements

PII, SMcL, JER, GM have been supported through National Science Foundation CAREER award #1843676.

Author Contributions Conceptualization: J.E.R, G.M., P.I.I.; Methodology: J.E.R, D.W, P.I.I.; Formal analysis and investigation: P.I.I., S.McL., J.E.R., G.M.; Writing – original draft preparation: P.I.I., S. McL., J.E.R.; Writing – review and editing: P.I.I., J.E.R, D.W., G.M.; Funding acquisition: J.E.R.; Resources: J.E.R., G.M., D.W.; Supervision: J.E.R., G.M. All authors reviewed the manuscript.

Funding

P.I. Ioannidi, S. McLafferty, J.E. Reber, and G. Morra have been supported through National Science Foundation CAREER award #1843676.

Data Availability

Supplementary Information including photos and videos from the analog experiments, raw data files, scripts and videos from the numerical simulations are stored here: https://doi.org/10.25380/iastate.24061518.

Declarations

Conflict of interest The authors have no relevant financial or non-financial interests to disclose.

Appendix

Supplemental Table

See Table 4.

Table 4

Supplemental table for analog experiments

HydroOrb property	Colorless HydroOrbs		Colorful HydroOrbs		
	DI water	Tap water	DI water	Tap water	Large orbs
Size/diameter (cm)	1.69 ± 0.09	1.41 ± 0.06	1.66 ± 0.08	1.43 ± 0.08	3.87 ± 0.25
Volume (cm^3)	2.55 ± 0.44	1.47 ± 0.19	2.43 ± 0.34	1.54 ± 0.30	31.76 ± 8.27
Mass (g)	2.88 ± 0.29	1.76 ± 0.14	2.46 ± 0.34	1.71 ± 0.18	38.12 ± 11.27
Density (g/cm^3)	1.06 ± 0.06	1.09 ± 0.08	1.07 ± 0.05	1.07 ± 0.07	1.04 ± 0.06
Poisson's ratio	0.41 ± 0.08	0.20 ± 0.05	0.38 ± 0.06	0.33 ± 0.06	0.37 ± 0.07
Young's modulus (kPa)	136.88 ± 67.64	197.00 ± 97.68	107.55 ± 41.03	91.47 ± 33.12	43.68 ± 23.16
Shear modulus (kPa)	48.54 ± 23.99	81.29 ± 41.29	37.80 ± 16.08	34.65 ± 12.54	16.78 ± 8.55
Yield force (N)					
Non-punctured	21.40 ± 4.03	20.53 ± 5.31	16.01 ± 4.43	13.79 ± 6.89	27.30 ± 12.13
Punctured	5.09 ± 2.63	3.98 ± 2.53	4.89 ± 2.96	3.56 ± 2.42	9.52 ± 4.15
Area of force application (cm^2)					
Non-punctured	2.96 ± 0.54	2.61 ± 0.28	1.97 ± 0.19	2.05 ± 0.15	18.07 ± 6.20
Punctured	2.00 ± 0.37	1.86 ± 0.29	1.91 ± 0.37	1.62 ± 0.36	13.47 ± 5.21
Yield stress (kPa)					
Non-punctured	72.27 ± 18.86	78.55 ± 21.93	57.08 ± 38.27	43.09 ± 22.56	15.01 ± 14.37
Punctured	25.44 ± 13.96	21.43 ± 13.81	25.62 ± 16.27	21.97 ± 15.70	7.07 ± 12.79

Summary table of HydroOrb Properties. One standard deviation listed after ± symbol

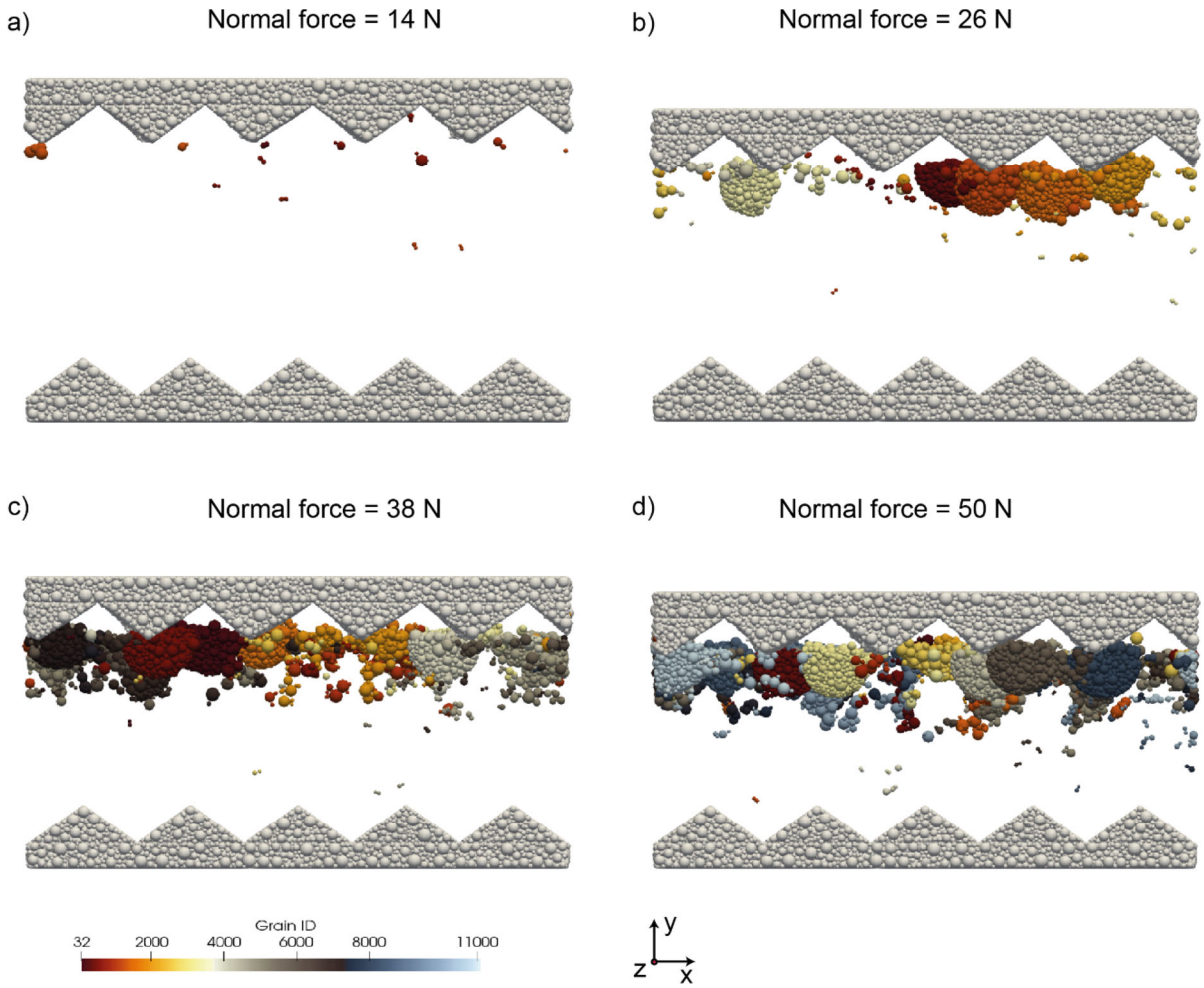

Figure 10
Visualization of the broken grains only, for models with varying normal force (14–50 N) at the end of each simulation. With increasing normal force, more microparticles are extracted from their parent grains, either as individual grains or as aggregates of smaller grains. These microparticles are then transported towards the center of the domain, and rarely passing the middle

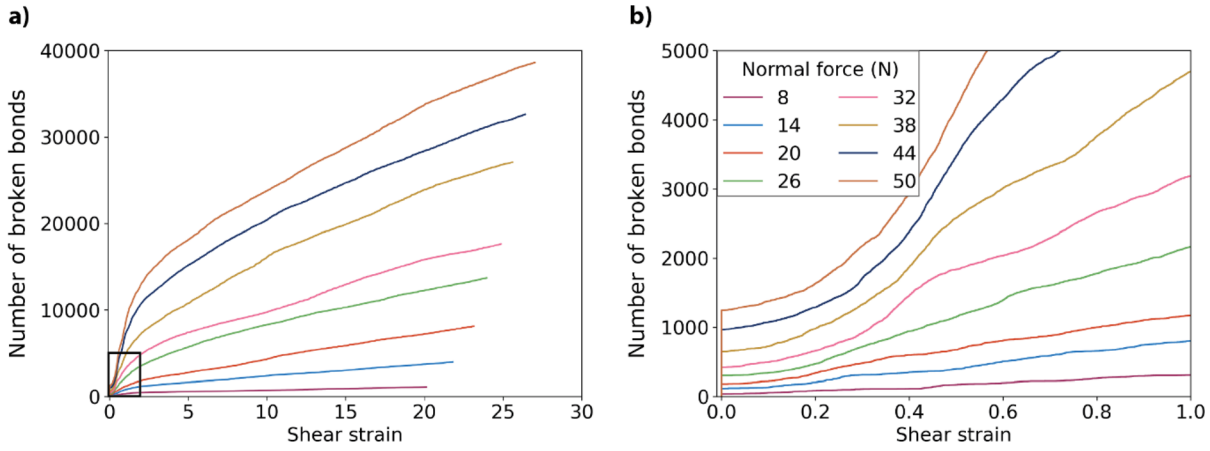

Figure 11
a Number of micro-particle bonds breaking with shear strain, for models with varying normal forces. Black box at the beginning of shearing is a zoom in shown in panel **b**. Note the vertical line at 0 shear strain, which represents the broken bonds before the onset of shearing, hence attributed to the vertical compaction during the first stage of the numerical models

Numerical Time Step and High-Mass/Density Approximation

The following formula gives the minimum stable time step, *dt*, for DEM models:

$$dt \leq 0.1\sqrt{(\mathrm{M}_{min}/\mathrm{K}_{\max})}$$
$$= 0.1 * \sqrt{(4/3 * \rho * {R_{min}}^3/Y_{max}/R_{max})}$$

where M_{min} is the lowest mass (in kg), $\mathrm{K}_{\max} = Y_{max} * R_{max}$ is the largest stiffness (N/m), ρ is the density, R_{min} and R_{max} are the smallest and largest discrete element particle radii, respectively, and Y_{max} is the largest Young's modulus (Pa = N/m^2). By using 10^6 times larger masses, we can increase the minimum time step required for the calculations from 10^{-3} to 1 ms. Using this larger timestep, the numerical models presented required $\sim$ 3 days to execute utilizing 20 HPC cores per simulation. By contrast, without the high mass approximation, each simulation would take $\sim$ 3000 days to execute. Utilization of a greater number of HPC cores would not result in a significant decrease of execution time. As the number of HPC cores increases, the time spent communicating information between cores will increase relative to the time spent doing calculations. When the number of particles per core drops below $\sim$ 5000, communication time exceeds calculation time and no further reduction in execution time is possible. This arises due to the way that parallelization is implemented in ESyS-Particle.

Bond and Grain Breakage in Numerical Models

References

Abe, S., Dieterich, J. H., Mora, P., & Place, D. (2002). Simulation of the influence of rate- and state-dependent friction on the macroscopic behavior of complex fault zones with the lattice solid model. *Pure and Applied Geophysics, 159*(9), 1967–1983. https://doi.org/10.1007/s00024-002-8718-7

Abe, S., & Mair, K. (2005). Grain fracture in 3D numerical simulations of granular shear. *Geophysical Research Letters, 32*(5), L05305. https://doi.org/10.1029/2004GL022123

Abe, S., & Mair, K. (2009). Effects of gouge fragment shape on fault friction: New 3D modelling results. *Geophysical Research Letters, 36*(23), L23302. https://doi.org/10.1029/2009GL040684

Abe, S., Place, D., & Mora, P. (2004). A parallel implementation of the lattice solid model for the simulation of rock mechanics and earthquake dynamics. *Pure and Applied Geophysics, 161*(11–12), 2265–2277. https://doi.org/10.1007/s00024-004-2562-x

Aharonov, E., & Sparks, D. (2002). Shear profiles and localization in simulations of granular materials. *Physical Review E, 65*(5), 051302. https://doi.org/10.1103/PhysRevE.65.051302

Anthony, J. L., & Marone, C. (2005). Influence of particle characteristics on granular friction. *Journal of Geophysical Research, 110*(B8), B08409. https://doi.org/10.1029/2004JB003399

Birren, T., & Reber, J. E. (2019). The impact of rheology on the transition from stick-slip to creep in a semibrittle analog. *Journal of Geophysical Research: Solid Earth, 124*(3), 3144–3154. https://doi.org/10.1029/2018JB016914

Bocquet, L., Losert, W., Schalk, D., Lubensky, T. C., & Gollub, J. P. (2001). Granular shear flow dynamics and forces: Experiment and continuum theory. *Physical Review E, 65*(1), 011307. https://doi.org/10.1103/PhysRevE.65.011307

Brace, W. F., & Byerlee, J. D. (1966). Stick-slip as a mechanism for earthquakes. *Science, 153*(3739), 990–992. https://doi.org/10.1126/science.153.3739.990

Cain, R. G., Page, N. W., & Biggs, S. (2001). Microscopic and macroscopic aspects of stick-slip motion in granular shear. *Physical Review E, 64*(1), 016413. https://doi.org/10.1103/PhysRevE.64.016413

Cates, M. E., Wittmer, J. P., Bouchaud, J.-P., & Claudin, P. (1998). Jamming, force chains, and fragile matter. *Physical Review Letters, 81*(9), 1841–1844. https://doi.org/10.1103/PhysRevLett.81.1841

Chang, S., Kim, M., Oh, S., Min, J. H., Kang, D., Han, C., Ahn, T., Koh, W.-G., & Lee, H. (2018). Multi-scale characterization of surface-crosslinked superabsorbent polymer hydrogel spheres. *Polymer, 145*, 174–183. https://doi.org/10.1016/j.polymer.2018.04.073

Cundall, P. A., & Strack, O. D. L. (1979). A discrete numerical model for granular assemblies. *Géotechnique, 29*(1), 47–65. https://doi.org/10.1680/geot.1979.29.1.47

Daniels, K. E., & Hayman, N. W. (2008). Force chains in seismogenic faults visualized with photoelastic granular shear experiments. *Journal of Geophysical Research, 113*(B11), B11411. https://doi.org/10.1029/2008JB005781

de Arcangelis, L., Ciamarra, M. P., Lippiello, E., & Godano, C. (2011). Micromechanics and statistics of slipping events in a granular seismic fault model. *Journal of Physics: Conference Series, 319*(1), 012001. https://doi.org/10.1088/1742-6596/319/1/012001

Dijksman, J. A., Brodu, N., & Behringer, R. P. (2017). Refractive index matched scanning and detection of soft particles. *Review of Scientific Instruments, 88*(5), 051807. https://doi.org/10.1063/1.4983047

Fan, Y., & Hill, K. M. (2011). Theory for shear-induced segregation of dense granular mixtures. *New Journal of Physics*. https://doi.org/10.1088/1367-2630/13/9/095009

Frye, K. M., & Marone, C. (2002). The effect of particle dimensionality on Granular friction in laboratory shear zones. *Geophysical Research Letters, 29*(19), 22-1–22-24. https://doi.org/10.1029/2002GL015709

Gray, J. M. N., & Thornton, A. (2005). A theory for particle size segregation in shallow granular free-surface flows. *Proceedings of the Royal Society a: Mathematical, Physical and Engineering Sciences, 461*(2057), 1447–1473. https://doi.org/10.1098/rspa.2004.1420

Guo, Y., & Morgan, J. K. (2006). The frictional and micromechanical effects of grain comminution in fault gouge from distinct element simulations. *Journal of Geophysical Research: Solid Earth*. https://doi.org/10.1029/2005JB004049

James, J. D., Ludwick, J. M., Wheeler, M. L., & Oyen, M. L. (2020). Compressive failure of hydrogel spheres. *Journal of Materials Research, 35*(10), 1227–1235. https://doi.org/10.1557/jmr.2020.114

Ladd, C. R., & Reber, J. E. (2020). The effect of a liquid phase on force distribution during deformation in a granular system. *Journal of Geophysical Research: Solid Earth, 125*(8), 1–17. https://doi.org/10.1029/2020JB019771

Losert, W., Bocquet, L., Lubensky, T. C., & Gollub, J. P. (2000). Particle dynamics in sheared granular matter. *Physical Review Letters, 85*(7), 1428–1431. https://doi.org/10.1103/PhysRevLett.85.1428

Mair, K., & Abe, S. (2008). 3D numerical simulations of fault gouge evolution during shear: Grain size reduction and strain localization. *Earth and Planetary Science Letters, 274*(1–2), 72–81. https://doi.org/10.1016/j.epsl.2008.07.010

Mair, K., & Abe, S. (2011). Breaking up: Comminution mechanisms in sheared simulated fault gouge. *Pure and Applied Geophysics, 168*(12), 2277–2288. https://doi.org/10.1007/s00024-011-0266-6

Mair, K., Frye, K. M., & Marone, C. (2002). Influence of grain characteristics on the friction of granular shear zones. *Journal of Geophysical Research: Solid Earth, 107*(B10), ECV 4-1-ECV 4-9. https://doi.org/10.1029/2001JB000516

Mair, K., & Hazzard, J. F. (2007). Nature of stress accommodation in sheared granular material: Insights from 3D numerical modeling. *Earth and Planetary Science Letters, 259*(3–4), 469–485. https://doi.org/10.1016/j.epsl.2007.05.006

Makedonska, N., Sparks, D. W., Aharonov, E., & Goren, L. (2011). Friction versus dilation revisited: Insights from theoretical and numerical models. *Journal of Geophysical Research, 116*(B9), B09302. https://doi.org/10.1029/2010JB008139

Marone, C., & Scholz, C. H. (1989). Particle-size distribution and microstructures within simulated fault gouge. *Journal of Structural Geology, 11*(7), 799–814. https://doi.org/10.1016/0191-8141(89)90099-0

May, L. B. H., Golick, L. A., Phillips, K. C., Shearer, M., & Daniels, K. E. (2010). Shear-driven size segregation of granular materials: Modeling and experiment. *Physical Review E—Statistical, Nonlinear, and Soft Matter Physics*. https://doi.org/10.1103/PhysRevE.81.051301

McLafferty, S., Bix, H., Bogatz, K., & Reber, J. E. (2023). New ring shear deformation apparatus for three-dimensional multiphase experiments: First results. *Egusphere. Instrum. Method. Data Syst*, *12*, 141–154. https://doi.org/10.5194/gi-12-141-2023

Mora, P., & Place, D. (1993). A lattice solid model for the nonlinear dynamics of earthquakes. *International Journal of Modern Physics C, 04*(06), 1059–1074. https://doi.org/10.1142/S0129183193000823

Mora, P., & Place, D. (1994). Simulation of the frictional stick-slip instability. *Pure and Applied Geophysics, 143*(1–3), 61–87. https://doi.org/10.1007/BF00874324

Mora, P., & Place, D. (1998). Numerical simulation of earthquake faults with gouge: Toward a comprehensive explanation for the heat flow paradox. *Journal of Geophysical Research: Solid Earth, 103*(B9), 21067–21089. https://doi.org/10.1029/98JB01490

Morgan, J. K., & Boettcher, M. S. (1999). Numerical simulations of granular shear zones using the distinct element method: 1. Shear

zone kinematics and the micromechanics of localization. *Journal of Geophysical Research: Solid Earth, 104*(B2), 2703–2719. https://doi.org/10.1029/1998JB900056

Mueth, D. M., Debregeas, G. F., Karczmar, G. S., Eng, P. J., Nagel, S. R., & Jaeger, H. M. (2000). Signatures of granular microstructure in dense shear flows. *Nature, 406*(6794), 385–389. https://doi.org/10.1038/35019032

Place, D., & Mora, P. (1999). The lattice solid model to simulate the physics of rocks and earthquakes: Incorporation of friction. *Journal of Computational Physics, 150*(2), 332–372. https://doi.org/10.1006/jcph.1999.6184

Place, D., & Mora, P. (2001). A random lattice solid model for simulation of fault zone dynamics and fracture process. In H. B. Mühlhaus, A. V. Dyskin, & E. Pasternak (Eds.), *Bifurcation and localization theory for soil and rock 99.* AA Balkeman.

Pouliquen, O., & Gutfraind, R. (1996). Stress fluctuations and shear zones in quasistatic granular chute flows. *Physical Review E, 53*(1), 552–561. https://doi.org/10.1103/PhysRevE.53.552

Rathbun, A. P., Renard, F., & Abe, S. (2013). Numerical investigation of the interplay between wall geometry and friction in granular fault gouge. *Journal of Geophysical Research: Solid Earth, 118*(3), 878–896. https://doi.org/10.1002/jgrb.50106

Reber, J. E., Hayman, N. W., & Lavier, L. L. (2014). Stick-slip and creep behavior in lubricated granular material: Insights into the brittle-ductile transition. *Geophysical Research Letters, 41*(10), 3471–3477. https://doi.org/10.1002/2014GL059832

Reber, J. E., Lavier, L. L., & Hayman, N. W. (2015). Experimental demonstration of a semi-brittle origin for crustal strain transients. *Nature Geoscience, 8*(9), 712–715. https://doi.org/10.1038/ngeo2496

Shojaaee, Z., Brendel, L., Török, J., & Wolf, D. E. (2012). Shear flow of dense granular materials near smooth walls. II. Block formation and suppression of slip by rolling friction. *Physical Review E, 86*(1), 011302. https://doi.org/10.1103/PhysRevE.86.011302

Sibson, R. H. (1977). Fault rocks and fault mechanisms. *Journal of the Geological Society, 133*(3), 191–213. https://doi.org/10.1144/gsjgs.133.3.0191

Siman-Tov, S., & Brodsky, E. E. (2018). Gravity-independent grain size segregation in experimental granular shear flows as a mechanism of layer formation. *Geophysical Research Letters, 45*(16), 8136–8144. https://doi.org/10.1029/2018GL078486

Stephens, D. J., & Bridgwater, J. (1978). The mixing and segregation of cohesionless particulate materials part II. Microscopic mechanisms for particles differing in size. *Powder Technology, 21*(1), 29–44. https://doi.org/10.1016/0032-5910(78)80105-3

Veje, C. T., Howell, D. W., & Behringer, R. P. (1999). Kinematics of a two-dimensional granular Couette experiment at the transition to shearing. *Physical Review E, 59*(1), 739–745. https://doi.org/10.1103/PhysRevE.59.739

Wang, Y., Abe, S., Latham, S., & Mora, P. (2006). Implementation of particle-scale rotation in the 3-D lattice solid model. *Pure and Applied Geophysics, 163*(9), 1769–1785. https://doi.org/10.1007/s00024-006-0096-0

Wu, L., Chen, G., Xing, J., & Lin, Z. (2022). Brittle cataclastic process of fault rocks based on a large-displacement direct shear model realized with DEM. *Journal of Structural Geology, 161*, 104641. https://doi.org/10.1016/j.jsg.2022.104641

(Received September 12, 2023, revised February 5, 2024, accepted March 8, 2024, Published online April 25, 2024)